Energy Storage Materials 66 (2024) 103200

Contents lists available at ScienceDirect

Energy Storage Materials

journal homepage: www.elsevier.com/locate/ensm

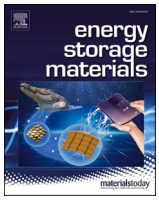

Unified understanding and mitigation of detrimental phase transition in cobalt-free $LiNiO_2$

Itsuki Konuma [a,†], Naohiro Ikeda [a,†], Benoît D.L. Campéon [b,c], Hinata Fujimura [a], Jun Kikkawa [d], Huu Duc Luong [d], Yoshitaka Tateyama [d], Yosuke Ugata [a,b], Masao Yonemura [a], Toru Ishigaki [e], Taira Aida [f], Naoaki Yabuuchi [a,b,*]

[a] Department of Chemistry and Life Science, Yokohama National University, 79-5 Tokiwadai, Hodogaya-ku, Yokohama, Kanagawa 240-8501, Japan
[b] Advanced Chemical Energy Research Center, Institute of Advanced Sciences, Yokohama National University, 79-5 Tokiwadai, Hodogaya-ku, Yokohama, Kanagawa 240-8501, Japan
[c] University Grenoble Alpes, University Savoie Mont Blanc, CNRS, Grenoble INP, LEPMI, Grenoble, France
[d] National Institute for Materials Science (NIMS), Namiki, Tsukuba, Ibaraki 305-0044, Japan
[e] Neutron Industrial Application Promotion Center, Comprehensive Research Organization for Science and Society (CROSS), Ibaraki Quantum Beam Center, 162-1 Shirakata, Tokai, Naka, Ibaraki 319-1106, Japan
[f] Sumitomo Metal Mining Co. Ltd., Battery Research Laboratories, 17-3, Isoura-cho, Nihama, Ehime 792-0002, Japan

ARTICLE INFO

Keywords:
Lithium nickelate
Phase transition
Nickel migration
Structural disordering

ABSTRACT

Ni-enriched layered materials are used as electrode materials of Li-ion batteries for electric vehicle applications. Stoichiometric $LiNiO_2$ with cationic Ni^{3+}/Ni^{4+} redox is the ideal electrode material, but the gradual loss of capacity at the high voltage region, associated with Ni ion migration, hinders its use for practical applications. Therefore, to improve electrode reversibility of $LiNiO_2$, less abundant Co ions and/or other electrochemically inactive ions, *e.g.*, Al^{3+} ions, are in part substituted for Ni ions. Nevertheless, a unified understanding of improvement by metal substitution is as yet not established. In this study, the origin causing detrimental phase transition in $LiNiO_2$ is discussed through the detailed analysis on $LiNiO_2$ integrated with nanosized Li_3PO_4 derived from a metastable and rocksalt $LiNiO_2$–Li_3PO_4 solid solution sample. $LiNiO_2$ derived from the metastable rocksalt oxide has approximately 6 % anti-site defects, and the particle size growth is suppressed by uniformly dispersed nanosized Li_3PO_4. In low crystallinity $LiNiO_2$ with partial structural disordering, the Ni ion migration to tetrahedral sites is effectively suppressed because of repulsive electrostatic interaction from Ni ions in Li layers. Moreover, from these findings, non-stoichiometric $Li_{0.975}Ni_{1.025}O_2$ with smaller particle size has been directly synthesized without high-energy milling and Li_3PO_4 integration, and significant improvement of electrode reversibility is achieved. Electrode reversibility of non-stoichiometric $Li_{0.975}Ni_{1.025}O_2$ is further improved through surface stabilization in a highly concentrated electrolyte solution. The unified understanding of deterioration mechanisms for $LiNiO_2$ offers a new criterion to design Co-free $LiNiO_2$ without metal substitution, leading to full utilization of a reversible capacity for layered materials.

The demand for electric vehicles equipped with Li-ion batteries is growing to develop low carbon society. Layered oxides are widely used for Li-ion battery applications since the historic inception of $LiCoO_2$ [1]. $LiCoO_2$, which has higher volumetric energy density, is a suitable electrode material for portable electronics. However, the limited supply chain of Co is a bottleneck for large scale batteries, like electric vehicle applications [2,3]. Instead, $LiNiO_2$, which is isostructural with $LiCoO_2$, is the ideal Co-free electrode material for large scale applications [4–9]. However, electrode reversibility is gradually lost on continuous electrochemical cycles even though the reversible capacity for the initial cycle exceeds 220 mA h g^{-1}. Ni ions are, therefore, partially substituted by other metal ions (Co, Mn, Al, Mg *etc.*) [10–12]. These materials are called "Ni-enriched layered materials" and are used as positive electrode materials for electric vehicle applications. Sun *et al.*, reported that 10 % Mn substitution for Ni ions, $LiNi_{0.9}Mn_{0.1}O_2$, is an effective approach to improve reversibility as electrode materials [13]. Dahn's group was also

* Corresponding author.
E-mail address: yabuuchi-naoaki-pw@ynu.ac.jp (N. Yabuuchi).
† These authors contributed equally to this work.

https://doi.org/10.1016/j.ensm.2024.103200
Received 17 October 2023; Received in revised form 2 January 2024; Accepted 14 January 2024
Available online 15 January 2024

reported that Al substitution in $LiNiO_2$ is beneficial to improve the electrode reversibility [14,15]. These approaches realize the development of "Co-free" batteries with Ni-enriched electrode materials. However, its origin of improvement by metal substitution is not clarified yet. Recently, the origin of deterioration of stoichiometric $LiNiO_2$ on electrochemical cycles has been discussed, which partly originates from the migration of Ni ions to tetrahedral sites in Li layers on full delithiation [16]. Although this process is reversible, the reversibility is gradually lost on continuous cycles. This fact leads to the continuous loss of reversible capacity at a high voltage region (4.1 – 4.3 V). The capacity associated with a phase transition at the high voltage region (often denoted as H2 – H3 phase transition [17]) is completely lost after 30 cycles at a rate of 10 mA h g^{-1} because Ni ions are left at the tetrahedral sites in Li layers [16]. This trend is clearly different from a phase transition observed for $LiCoO_2$ on full delithiation [16,18]. Co ion migration is not observed for $LiCoO_2$, and instead the cooperative glide of CoO_2 slabs is observed [19]. This phase transition results in the formation of layered CoO_2, which is isostructural with CdI_2 with space group *P*-3*m*1.

Recently, Sun *et al*. reported that tungsten (W) doping in $LiNiO_2$ is an efficient approach to suppress the detrimental phase transitions at high-voltage region, and it has been reported that electrode reversibility is improved only by 1.5 mol% of W doping, and they have structurally analyzed the sample by assuming the formation of solid solution, *i.e.*, $LiNi_{0.985}W_{0.015}$ [20,21]. Nevertheless, W ions are easily oxidized to the hexavalent state, and therefore solid solution formation with $LiNiO_2$ is expected to be energetically unfavorable. In addition, the W doping significantly reduces crystallinity, and the peak intensity of 104 diffraction line is increased relative to 003 diffraction line [21]. This finding suggests the partial Ni ion occupation in the Li layer of $LiNiO_2$ if it is assumed that the solid solution phase with W ions is not formed. Indeed, Dahn *et al*. have reported that W addition leads to phase segregation of W ions and enrichment of W ions in grain boundaries of $LiNiO_2$ [22]. On the basis of this recent finding, it is hypothesized that heavy and expensive W ions can be substituted by other elements, which do not form solid solution with $LiNiO_2$. In this study, to test this hypothesis, phosphorus, which is a lighter and more abundant element, is targeted. As a stable Li salt with phosphorus, Li_3PO_4 is selected and integrated with $LiNiO_2$. A crystal structure of Li_3PO_4 is classified as a Wurtzite-derived structure, and Li^+ and P^{5+} ions are located at tetrahedral sites in the hexagonal close-packed (hcp) lattice of oxide ions. Therefore, a low structural compatibility with $LiNiO_2$, consisting of cubic close-packed (ccp) lattice of oxide ions with Li^+ and Ni^{3+} ions at octahedral sites, is anticipated. Recently, our group has reported that solid solution between Li_3PO_4 and $LiMnO_2$, which have a low structural compatibility, is formed by high-energy mechanical milling [23]. Metastable and nanosized oxides with a disordered rocksalt structure is successfully obtained from a mixture of Li_3PO_4 and $LiMnO_2$. Heat treatment of the metastable oxide results in the phase segregation into Li_3PO_4 and $LiMnO_2$ with nanosized particles, and both phases are uniformly dispersed at nanoscale.

In this study, this methodology is extended to $LiNiO_2$ by successfully integrating nanosized Li_3PO_4 into $LiNiO_2$ at the nanoscale. Electrode reversibility is significantly improved by the addition of only 3 mol% of Li_3PO_4 into $LiNiO_2$ associated with the partial suppression of Ni migration into tetrahedral sites on full delithiation. Structural analysis by synchrotron X-ray and neutron diffraction reveals that the non-negligible amount of anti-site defect with lower crystallinity is formed, which effectively suppresses Ni migration because of large repulsive electrostatic interaction from Ni ions located in Li layers. Moreover, this finding suggests that Li_3PO_4 is not necessary for the suppression of the unfavorable phase transition, and therefore, non-stoichiometric Li_yNiO_2 with partial Ni ion occupation in transition metal layers has been synthesized without high-energy milling and Li_3PO_4 integration. Indeed, non-stoichiometric Li_yNiO_2 without Li_3PO_4 shows good electrode reversibility without the addition of non-nickel ions and the loss of reversible capacity at high-voltage region. This finding opens a new direction to develop high performance and practical Co-free Ni-based electrode materials with extremely simple and cost-effective methodology.

The uniform mixing of $LiNiO_2$ *and nanosized* Li_3PO_4 *by a post heat-treatment technique*: A synthesis methodology of $LiNiO_2$ mixed with nanosized Li_3PO_4 is described in Fig. 1. Firstly, $LiNiO_2$ and 3 mol% Li_3PO_4 was thoroughly mixed by high-energy mechanical milling at 600 rpm (Fig. 1, step 1). Nearly stoichiometric $LiNiO_2$ was synthesized with the same methodology reported by Sun et al. [7], which is further mixed with Li_3PO_4 by high-energy ball milling (also see experimental section). After mechanical milling, a nanosized oxide with a disordered rocksalt structure is successfully obtained as shown in Fig. 1, step 2. X-ray diffraction (XRD) patterns and particle morphology of $LiNiO_2$ and Li_3PO_4 are completely lost, and uniform distribution of Ni and P ions is evidenced from EDX maps in Supporting Figure S1. Dissolution of PO_4^{3-} ions into rocksalt phase by mechanical milling is also evidenced for the $LiMnO_2$–Li_3PO_4 system through combination study of experimental and theoretical approaches [23]. The formation of a solid solution phase, similar to $LiMnO_2$, is anticipated in $LiNiO_2$. Electrode performance of $LiNiO_2$ before and after milling with 3 mol% Li_3PO_4 is shown in Supporting Fig. 2. The as-prepared rocksalt oxide with 3 mol% Li_3PO_4 shows a smaller reversible capacity with larger irreversible capacity for the initial cycle, which is expected to originate from electrolyte decomposition on the active surface of nanosized rocksalt oxide with Ni ions formed by high-energy mechanical milling (an FE-SEM image is found in Fig. 1, step 2). Anionic redox is activated for Ni-based oxides with the disordered rocksalt structure [24], and anionic redox would be destabilized for nanosized and rocksalt $LiNiO_2$ with larger surface area.

Because the low crystallinity oxide with the rocksalt structure shown in Fig. 1, step 2 is a metastable phase, phase segregation occurs after heating, leading to phase transition to thermodynamically stable phases. As displayed in Supporting Figure S3, the metastable rocksalt oxide is stable below 300 °C, and a partially cation ordered layered phase is formed at 450 °C. The layered phase is finally formed by heating at a higher temperature of 650 °C for 6 h. Changes in electrode reversibility on heating to 650 °C are also shown **Supporting Figure S4**. Only a small improvement is achieved after heating at 300 and 450 °C whereas a reversible capacity of >200 mA h g^{-1} is obtained after heating at 650 °C. After heat-treatment, the growth of particle size is noted as shown in Fig. 1, step 3, but the average particle size (approximately 90 nm) is considerably smaller compared with as-prepared $LiNiO_2$ (approximately 260 nm). FE-SEM images with different magnifications for these samples are also found in **Supporting Figure S5**. In addition, STEM-EDX study reveals that P ions are uniformly distributed with Ni ions, but the presence of some P-enriched regions is also found in the EDX spectra and P map. The detailed crystal structure of the sample was further examined by synchrotron XRD and neutron diffraction (ND) study, and the results are compared with as-prepared $LiNiO_2$ without Li_3PO_4. From the synchrotron XRD patterns, two important findings are noted. For as-prepared $LiNiO_2$, small amount of Li_2CO_3 is observed as found in the enlarged XRD patterns in the range of 7 – 11° (Fig. 2a) [17,25]. Clear peak splitting of 108 and 110 diffraction lines is also evidenced, indicating higher crystallinity with the layered structure. In contrast, significantly lower crystallinity for $LiNiO_2$ with Li_3PO_4 is noted, and peak splitting of 108 and 110 diffraction lines is not clear. Peak widths of diffraction patterns are quite broader for $LiNiO_2$ with Li_3PO_4. The presence of crystalline Li_3PO_4 is also found in the enlarged pattern. From ND patterns, the peak intensity of 003 diffraction line relative to 104 diffraction line is clearly weakened for $LiNiO_2$ with Li_3PO_4 (Fig. 2b), which is clearly more pronounced for ND data when compared with XRD data. Rietveld analysis of the ND pattern for as-prepared $LiNiO_2$ reveals that the occupation of Ni ions in Li layer is less than 2 % as shown in refined structural parameters in Fig. 2b. A similar trend is noted by Rietveld analysis of the synchrotron XRD pattern (**Supporting Figure S6**). In contrast, the weak peak intensity for 003 line in the ND pattern of $LiNiO_2$ with Li_3PO_4 indicates a more clear Ni occupation in Li layer.

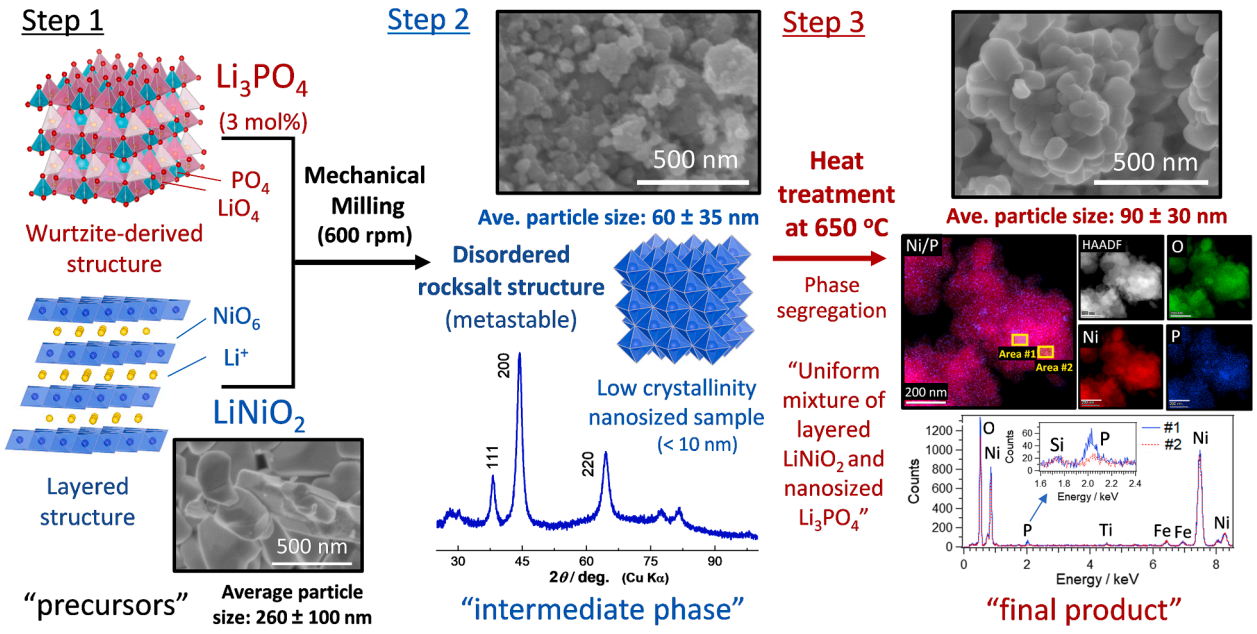

Fig. 1. Scheme of the synthesis procedure of $LiNiO_2$ integrated with nanoscale Li_3PO_4: Also see the text for experimental details for each step. Particle sizes of samples obtained with different experimental steps are also shown. Layered $LiNiO_2$ integrated with Li_3PO_4 was characterized by STEM-EDX technique. Schematic illustrations of crystal structures were drawn using the VESTA program [55].

Herein, two models are applied for the structural analysis. One is an anti-site defect model, *i.e.*, $(Li_{1-x}Ni_x)_{3b}(Li_xNi_{1-x})_{3a}O_2$, and another is an excess Ni model, *i.e.*, $(Li_{1-x}Ni_x)_{3b}Ni_{3a}O_2$. The excess Ni model was applied for the analysis of $LiNiO_2$ synthesized at higher temperatures or Li deficient conditions [26]. The anti-site defect model was adapted from $LiNi_{1/2}Mn_{1/2}O_2$ [27]. Although it is difficult to distinguish both models from XRD patterns (**Supporting Figure S7**), the analysis of the ND pattern suggests that the sample possesses anti-site defects (**Supporting Figure S8**). Because this sample is crystallized from the precursor with the cation disordered rocksalt structure and enriched anti-site defects, this finding is also consistent with this fact. Approximately 6 % of anti-site defects are formed in $LiNiO_2$ derived from the nanosized rocksalt phase (Fig. 2b). Note that similar observation, lowered crystallinity and peak intensity changes, is also noted for W doped $LiNiO_2$ [21,22].

The distribution of Li_3PO_4 into $LiNiO_2$ was further studied by cross-sectional STEM observation. As shown in Fig. 2c, a clear contrast in color is found for $LiNiO_2$ with Li_3PO_4, and EDX mapping reveals that Li_3PO_4 is enriched in lighter color regions (**Supporting Figure S9**). Although Li_3PO_4-rich regions are present, nanosized Li_3PO_4 particles are uniformly distributed inside particles between $LiNiO_2$ grains. Because Li_3PO_4 and $LiNiO_2$ are immiscible for each other, the growth of particle size of $LiNiO_2$ is effectively suppressed on heating, leading to the formation of nanosized $LiNiO_2$. Therefore, grain size is clearly smaller for $LiNiO_2$ with Li_3PO_4 when compared with as-prepared $LiNiO_2$. Grain morphology is also different for both samples, rectangular-shaped grains for as-prepared $LiNiO_2$ are lost for the sample with Li_3PO_4, which is similar to round-shaped grains for disordered rocksalt $LiNiO_2$. Smaller grain size was also found for W doped $LiNiO_2$ [22]. In conclusion, $LiNiO_2$ derived from disordered rocksalt $LiNiO_2$ with 3 mol% Li_3PO_4, has the following characteristics; (1) approximately 6 % of anti-site defects for Li/Ni sites, (2) smaller particle sizes and lower crystallinity compared with $LiNiO_2$ without Li_3PO_4, and (3) uniform integration with nanosized Li_3PO_4.

Comparison of Li storage reversibility of $LiNiO_2$ *with or without* Li_3PO_4: Detailed electrode performance of $LiNiO_2$ derived from disordered rocksalt $LiNiO_2$ with 3 mol% Li_3PO_4 was further examined, and results are summarized in Fig. 3. $LiNiO_2$ without Li_3PO_4 shows the highest initial discharge capacity of 220 mA h g^{-1} at a rate of 10 mA g^{-1}, but the capacity is continuously decreased on continuous cycles. A reversible capacity of 60 mA h g^{-1} is lost after 30 cycles as shown in **Supporting Figure S10**. In contrast, as shown in Fig. 3a, the capacity of $LiNiO_2$ with Li_3PO_4 gradually increases and reaches the maximum value of 220 mA h g^{-1} around 15th cycle (**Supporting Figure S10**). The gradual increment of reversible capacities is discussed in the later section. Although the discharge capacity is gradually reduced on further cycles, considerably better capacity retention is achieved. A similar trend is also observed under accelerated cycle test at 50 mA g^{-1}, and significantly better capacity retention is realized after 100 cycles for $LiNiO_2$ with Li_3PO_4 (Fig. 3b). Note that the initial discharge capacity is relatively small for $LiNiO_2$ with Li_3PO_4, which originates from the presence of electronically non-conductive Li_3PO_4. Indeed, when 5 mol% Li_3PO_4 is integrated with $LiNiO_2$, an obvious capacity loss is observed, and no improvement of capacity retention is found in Supporting Figure S11. In addition, some extent of improvement is observed for 1 mol% Li_3PO_4, but lower capacity retention is evidenced after 30 cycle test (**Supporting Figure S11**). $LiNiO_2$ with Li_3PO_4 also shows good rate capability in Fig. 3c, but slightly better rate capability is noted for $LiNiO_2$ without Li_3PO_4 in **Supporting Figure S12**.

Degradation mechanisms of $LiNiO_2$ with or without Li_3PO_4 were further studied by electrochemical measurements coupled with detailed structural analysis. As clearly shown in dQ/dE curves of $LiNiO_2$ without Li_3PO_4, the phase transition at the high voltage region of 4.2 V is gradually lost on cycles (Fig. 3d), which is a unique degradation mechanism related to the Ni migration to tetrahedral sites [16]. The presence of Ni ions in Li layers impede Li ion migration, and Li ions would be partly immobilized. This observation is also supported by the fact that the increase in impedance on continuous cycles (Fig. 3d inset). In contrast, the reversible phase transition at the high voltage region is achieved for $LiNiO_2$ with Li_3PO_4, and high reversibility is achieved even after 30 cycles at a rate of 10 mA g^{-1} (Fig. 3e). Moreover, the growth of impedance on electrochemical cycles is clearly mitigated under the same cycle conditions (Fig. 3e inset). The difference in degradation processes for both samples is further discussed in the following section.

Origin of the improvement of electrode reversibility for $LiNiO_2$ *with* Li_3PO_4: To further clarify the phase evolution process, *in-situ* XRD study and *ex-situ* synchrotron XRD studies of $LiNiO_2$ with or without Li_3PO_4 were conducted. Evolution of *in-situ* XRD patterns of $LiNiO_2$ with Li_3PO_4

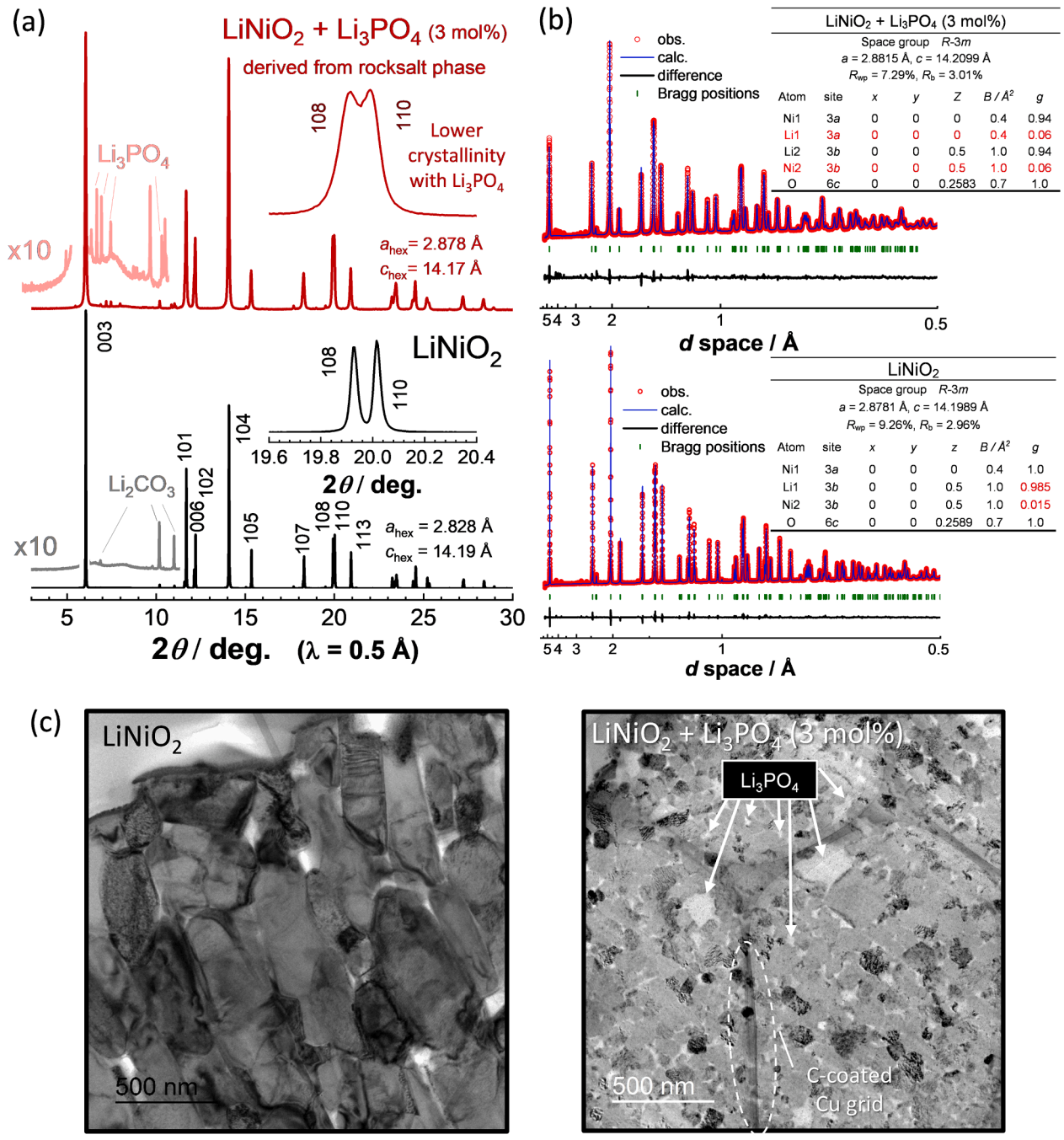

Fig. 2. Structural and morphological characterization of $LiNiO_2$ integrated with Li_3PO_4: (a) synchrotron XRD patterns of $LiNiO_2$ with or without Li_3PO_4. Enlarged patterns also shown for comparison. ND patterns and refined structural parameters obtained by Rietveld analysis is also shown in (b). Cross-sectional STEM images of both samples are also shown in (c).

is displayed in Fig. 4a and **Supporting Figure S13** and **S14**, and results are also compared with that of $LiNiO_2$ without Li_3PO_4 [16]. Two important findings for both samples are noted. (1) Expansion and shrinkage of interlayer distances are clearly suppressed for $LiNiO_2$ with Li_3PO_4, which is expected to originate from the presence of anti-site defects. Extra Ni ions in Li layers disturb the expansion and shrinkage of $Ni_{1-y}O_2$ slabs compared with stoichiometric $LiNiO_2$. Total changes in *d*-spacing are calculated to be 0.25 Å for the sample with Li_3PO_4 and 0.33 Å without Li_3PO_4 as shown in Fig. 4a. (2) The intensity of 101 diffraction line at 36.5 – 37.5° increases on full delithiation for both samples, which is indicative of Ni ion migration to tetrahedral sites [16]. However, the peak intensity is less intensified for $LiNiO_2$ with Li_3PO_4. This trend is further visualized in *ex-situ* synchrotron XRD patterns for both samples after full delithiation and after 20 cycles in Fig. 4**b**. After charge to 4.5 V in a Li cell, 101 peak intensity is clearly intensified for $LiNiO_2$ without Li_3PO_4. Although relative peak height of 101 to 104 is also increased for $LiNiO_2$ with Li_3PO_4, the peak intensity is much smaller compared with $LiNiO_2$ without Li_3PO_4. This fact indicates that Ni migration to tetrahedral sites in Li layers is less pronounced for $LiNiO_2$ with Li_3PO_4. Peak broadening with an asymmetric peak profile at the fully charged sample suggests that two phases coexist. However, after discharge, a sharp peak profile again appears (Supporting Figure S15), indicating the phase transition, including partial Ni migration, is a highly reversible process. Ni migration on full delithiation may be also supported by X-ray absorption spectroscopy (XAS) as shown in **Supporting Figure S16**. Energy shift in Ni K-edge spectra to the lower

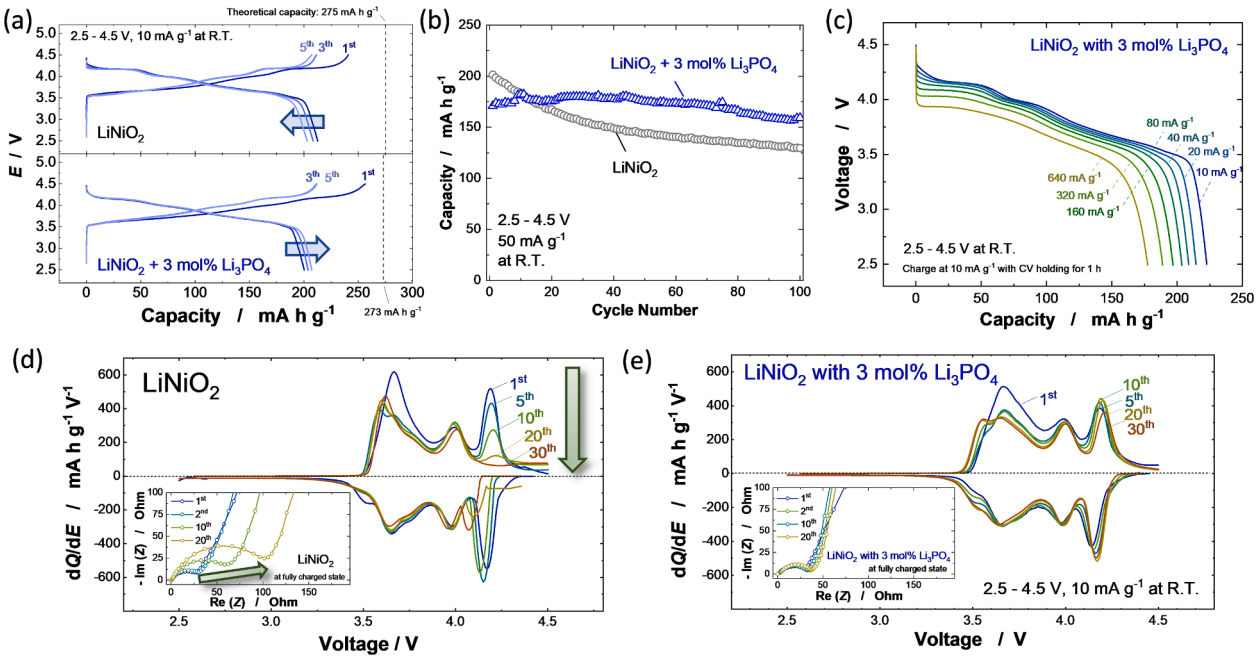

Fig. 3. Electrode performance of $LiNiO_2$ with and without Li_3PO_4 integration: (a) galvanostatic charge/discharge curves at a rate of 10 mA g^{-1} and (b) capacity retention at a rate of 50 mA g^{-1}. Rate-capability of $LiNiO_2$ integrated with Li_3PO_4 is shown in (c); sample loading for rate-capability test; 7.2 mg cm^{-2}. Differential capacity plots of both samples at a rate of 10 mA g^{-1} are also compared in (d, e). Evolution of impedance data for both samples are also shown in the inset.

energy region on charge from 180 to 260 mA h g^{-1} may be because of Ni ion migration to Li sites [28]. Moreover, the relative peak intensity between 101 and 104 diffraction lines after 20 cycles shows that the peak intensity of 101 is clearly increased for $LiNiO_2$ without Li_3PO_4 (Fig. 4b), and its Rietveld analysis reveals that approximately 9 % Ni ions are located at tetrahedral sites in Li layers (**Supporting Figure S17a**). In contrast, for the case of $LiNiO_2$ with Li_3PO_4, the change in peak intensity of 101 is suppressed before and after 20 cycles, suggesting that Ni ion migration reversibility is improved. Approximately 3 % of Ni ions are found after 20 cycles by Rietveld analysis (**Supporting Figure S17b**). The presence of Ni ions at tetrahedral sites is further visualized by maximum entropy method (MEM) for the synchrotron X-ray diffraction patterns. MEM analysis reveals that non-negligible electron density is found at tetrahedral sites in Li layers for both samples as shown in Fig. 4c. However, similar to Rietveld structural analysis, electron density at tetrahedral sites is clearly enriched for $LiNiO_2$ without Li_3PO_4. Note that the reversible capacity of the sample is gradually increased on electrochemical cycles (Fig. 3b and **Supporting Figure S10**). The increase in capacities would be expected to be correlated with Ni migration in Li layers. When the Ni ion concentration in Li layers is locally enriched, Li ions is immobilized. However, Ni ions in Li layers are mobile when Li ion vacancies are formed around Ni ions [29]. The Ni migration and re-distribution of Ni ions in Li layers would enrich active Li ions in the structure, leading to the increase in reversible capacity.

Because tetrahedral sites in Li layers face-share octahedral sites in Li layers, the presence of anti-site defects and Ni ion occupation in Li layers are expected to cause repulsive electrostatic interaction against Ni ion migration to tetrahedral sites [30]. This hypothesis was further evaluated by a computational approach. Two models for the charged sample with or without anti-site defects were adapted, *i.e.*, $[\square_{11/12}Ni_{1/12}]_{3a}[Li_{1/12}Ni_{11/12}]_{3b}O_2$ and $[\square_{11/12}Li_{1/12}]_{3a}[Ni]_{3b}O_2$. Herein, $\square$ denotes vacant octahedral sites formed by delithiation. In $[\square_{11/12}Li_{1/12}]_{3a}[Ni]_{3b}O_2$ without anti-site defects, Li ion at a tetrahedral site in the Li layer can activate Ni-ion migration from the NiO_2 layer to the tetrahedral site in the neighbor Li layer with the calculated activation energy of 1.66 eV, as shown in Fig. 4d (left). The transition state corresponds to Ni at the center of the oxygen triangle between Ni and Li layers. Such collective migration of Li and transition metal ions has been also reported in layered-type $Li_{1.2-y}Cr_{0.4}Mn_{0.4}O_2$ [31]. In the model with the anti-site defect in Fig. 4d (right), such Ni-ion migration (to the B site in the Li layer) can take place after the migration of the Ni ion in Li layer to the A site owing to the electrostatic repulsion between the two Ni ions. The activation energy of this type of Ni-ion migration is calculated to be 2.64 eV, which is much higher than the case without the anti-site defect. These results indicate that Ni ions in the NiO_2 layer are unlikely to migrate to the Li layer in the presence of the anti-site defects. Therefore, the formation of anti-site defects would effectively suppress the Ni ion migration to tetrahedral sites, leading to better reversibility as electrode materials.

Practical Methodology for Synthesis of Co-free $LiNiO_2$ *with Superior Electrode Reversibility*: Electrode reversibility of $LiNiO_2$ is significantly improved by Li_3PO_4 integration coupled with the formation of anti-site defects. These findings indicate the importance of anti-site defects in the improvement of electrode reversibility. However, the necessity of Li_3PO_4 which is found as a segregated phase, is not fully understood. Segregation of W ions is also evidenced in literature [22]. Anti-site defects are easily formed for $LiNiO_2$ when compared with $LiCoO_2$ [32]. The formation of anti-site defects is also observed for $LiNiO_2$ with low-level Zr doping [33], and for Ta-substituted Ni-rich system [34]. Similarly, W doping is also expected to induce anti-site defects formation from the peak intensity changes for 003/104 diffraction lines [21]. Although such anti-site defects affect the rate-capability of $LiNiO_2$ as electrode materials, this problem would be solved by the reduction of particle sizes and shortening of Li migration distances in oxide particles. Indeed, the growth of particle sizes is effectively suppressed by uniformly dispersed Li_3PO_4 as shown in Fig. 2c. For comparison, Li_3PO_4 coating was conducted on stoichiometric $LiNiO_2$ by using a methodology reported in literature [35]. As shown in **Supporting Figure S18**, no clear improvement of electrode reversibility is evidenced solely by Li_3PO_4 coating. These facts also suggest that particle size and anti-site defects would be indispensable, and the presence of Li_3PO_4 and other dopants are less responsible for the improvement of electrode reversibility.

To test this hypothesis, structural defects are induced for $LiNiO_2$, and $LiNiO_2$ was synthesized with 4 % Li deficient condition, *i.e.*, $Li_{0.96}NiO_2$. Synthesis protocol of Li deficient $LiNiO_2$ is summarized in Fig. 5a, and

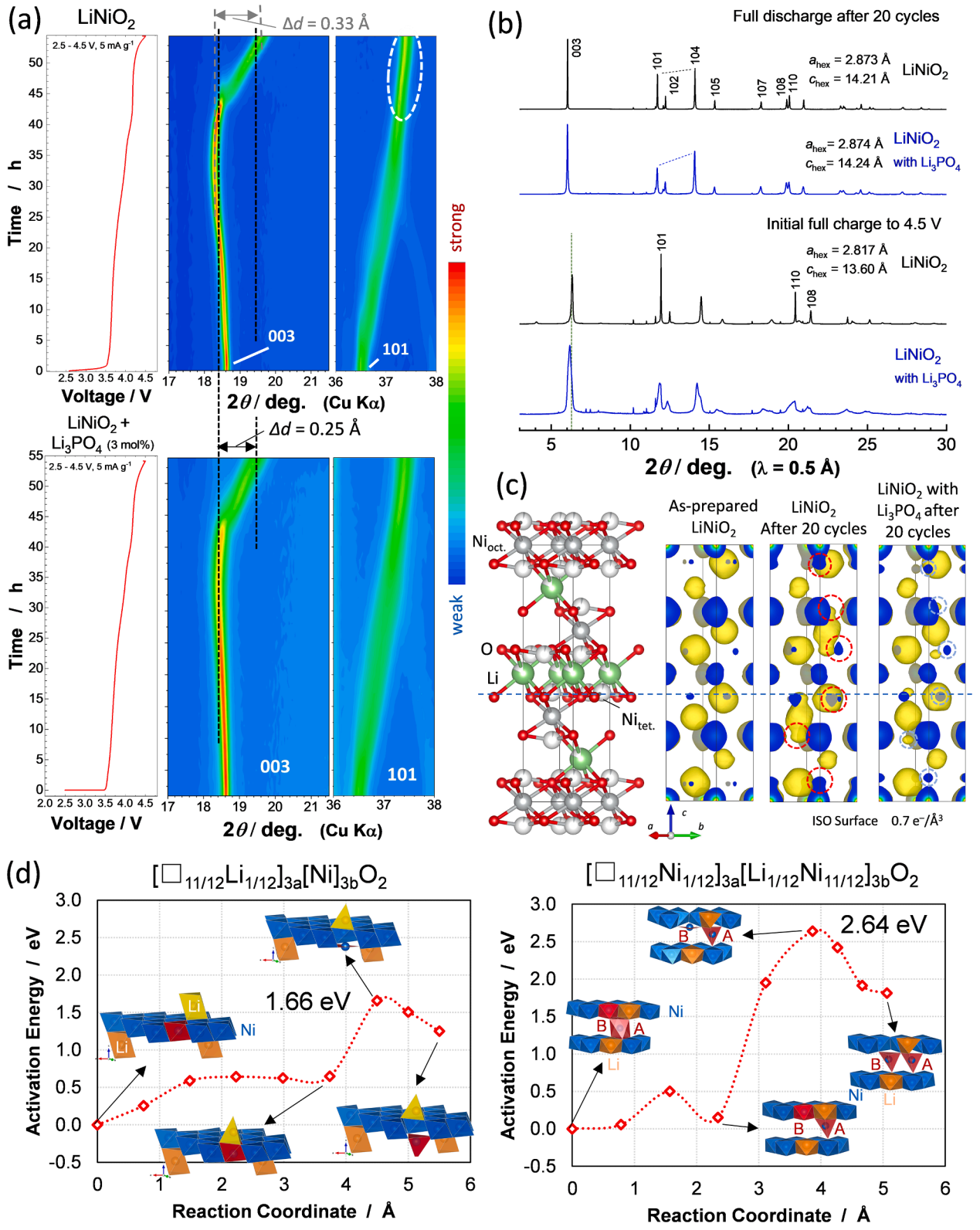

Fig. 4. Structural evolution and phase transition of $Li_{1-y}NiO_2$ with or without Li_3PO_4: (a) Contour plots for selected ranges obtained from the *in-situ* XRD patterns of $LiNiO_2$ integrated with or without Li_3PO_4 at a rate of 5 mA g^{-1}, and corresponding initial charge curves in electrochemical cells. The original *in-situ* XRD data of $LiNiO_2$ integrated with Li_3PO_4 are found in **Supporting Figure S13**. Contour plots with different angles are also shown in **Supporting Figure S14**. (b) *Ex-situ* synchrotron XRD data for $LiNiO_2$ with or without Li_3PO_4 integration after charge to 4.5 V and after 20 cycles. (c) Electron density distributions obtained by MEM method for $LiNiO_2$ before and after electrochemical cycles. (d) Theoretical study of Ni migration in $Li_{1-y}NiO_2$ with or without anti-site defects.

this sample can be obtained without high-energy ball milling, which is difficult to adapt for industrial-scale production. Particle growth is clearly suppressed for non-stoichiometric oxides (Fig. 5b and **Supporting Figure S19**), and average particle size is reduced to 110 nm, in comparison to 260 nm for stoichiometric $LiNiO_2$ (Fig. 1 and **Supporting Figure S5**). To further study the impact of Li deficiency on cation distributions for Li_xNiO_2, the Li deficiency is systematically changed within $1.00 \geq x \geq 0.90$. Structural changes for Li_xNiO_2 with different Li deficient conditions are shown in **Supporting Figure S20**. Peak height for 003 and 104 diffraction lines systematically changes as a function of Li contents, and peak height of 104 diffraction lines increases as Li contents decrease, which is indicative of the increase of Ni ion occupation in Li layers. For $Li_{0.96}NiO_2$, a small amount of Li_2CO_3 is found in the sample (Fig. 5b), and therefore, a chemical composition is expected to be slightly deviated from the ideal composition. In addition, if it is hypothesized that a cation vacancy is not formed, the chemical composition of the sample is expected to be "$Li_{0.975}Ni_{1.025}O_2$". This chemical composition is further validated by Rietveld structural analysis, and inconsistency is not found. The formation of anti-site defects is also directly found by the analysis of the neutron diffraction pattern of $Li_{0.975}Ni_{1.025}O_2$, and its cation distribution has been successfully refined as $[Li_{0.935}Ni_{0.065}]_{3b}[Li_{0.04}Ni_{0.96}]_{3a}O_2$ (**Supporting Figure S21**). Note that Li/Ni ordering is not observed for the Ni-rich phase, *e.g.*, $Li_{0.29}Ni_{0.71}O$, and a cation-disordered rocksalt phase is formed in $Li_{0.29}Ni_{0.71}O$ [36], indicating that $Li^+/Ni^{2+}/Ni^{3+}$ ions have a tendency to form a disordered arrangement. This fact also supports that anti-site defects are preferably formed in $Li_{0.975}Ni_{1.025}O_2$ rather than the formation of $LiNiO_2$–NiO solid solution with Li/Ni ordering (an excess Ni model). Similarly, the formation of anti-site defects is discussed and analyzed in $LiNi_{0.8}Mn_{0.1}Co_{0.1}O_2$ and anti-site defects are easily formed depending on synthesis conditions [37]. Particle sizes of samples are also influenced by Li contents (**Supporting Figure S19**). A small amount of Li_2CO_3 is found in $LiNiO_2$ (Fig. 2a), and the growth of particle size of $LiNiO_2$ is anticipated to be facilitated by the presence of Li_2CO_3 flux [38,39]. Therefore, the sample with a smaller particle size is obtained for Li less compositions and less Li_2CO_3 flux as shown in **Supporting Figure S19**.

$Li_{0.975}Ni_{1.025}O_2$ synthesized with a Li deficient condition was further tested as electrode materials (**Supporting Figure S22**). When electrode performance of $LiNiO_2$ and $Li_{0.975}Ni_{1.025}O_2$ were compared with 4.15 V cut-off, in which Ni migration cannot be observed, both samples show excellent capacity retention without voltage decay and no increase in polarization on continuous cycles, but a smaller reversible capacity (by approximately 15 mA h g^{-1}) is obtained for $Li_{0.975}Ni_{1.025}O_2$ at 50 mA g^{-1} (**Supporting Figure S22a**). This finding is clearly consistent with the general understanding of $LiNiO_2$. Electrode kinetics are negatively influenced by the presence of structural defects [40], which is also proved by *Ab initio* molecular dynamics simulations [29]. Li ion migration is impeded by the presence of extra Ni ions in Li layers. However, when the cut-off voltage is increased to 4.5 V, the suppression of voltage decay and capacity loss is clearly observed for $Li_{0.975}Ni_{1.025}O_2$ (**Supporting Figure S22b**). $Li_{0.975}Ni_{1.025}O_2$ shows comparable electrode performance with $LiNiO_2$ integrated with Li_3PO_4 as shown in **Supporting Figure S22c**. Moreover, electrode performance is further increased with a concentrated electrolyte solution, lithium bis(fluorosulfonyl)amide (LiFSA) dissolved in DMC (LiFSA:DMC = 1:1.1 in molar ratio) [41]. Superior chemical stability of LiFSA compared with $LiPF_6$ and the presence of non-free-solvent in concentrated electrolyte effectively suppress the increase in the impedance on continuous electrochemical cycles [41,42]. Reversibility of alkaline metal deposition/dissolution is also significantly improved for salts with FSA anion [43,44]. Higher electrode reversibility, including a high voltage region, is achieved with Li-deficient $Li_{0.975}Ni_{1.025}O_2$ and concentrated electrolyte with LiFSA. Higher viscosity is an critical issue as electrolyte, but this issue is effectively solved by adapting aramid-coated separator, which shows better wettability to highly concentrated electrolyte solutions [45,46]. To examine the influence of highly concentrated electrolyte solutions, firstly, $LiNiO_2$ was tested as the electrode material. Electrode performance is significantly improved as shown in Fig. 5c when compared with the result with conventional electrolyte at the same condition (Fig. 3b). Nearly 90 % of reversible capacity is retained after 100 cycles. Nevertheless, as shown in Fig. 5c inset, the increase in polarization at the higher voltage region is also clearly observed. This type of degradation is the essentially same as of $LiNiO_2$ cycled in a conventional electrolyte solution [16]. Recently, similar to our study, the improvement of reversibility of $LiNiO_2$ has been reported by using fluoroethylene carbonate and $LiPO_2F_2$ additive [47]. However, the increase in polarization at the high voltage region coupled with capacity loss cannot be eliminated. On charge, Ni ions migrate to tetrahedral sites, and Ni ion migration reversibility is influenced by the increase in polarization on discharge. The reversibility of Ni migration is, therefore, gradually lost on continuous cycles associated with a gradual increase in polarization at the high voltage region, and Ni ions are left at tetrahedral sites on continuous cycles, leading to the loss of capacity. In contrast, although the discharge capacity is slightly reduced (approximately 10 mA h g^{-1}), the increase in the polarization at the high voltage region is clearly mitigated for $Li_{0.96}NiO_2$ with highly concentrated electrolyte (Fig. 5d). Moreover, a clear correlation is found between capacity retention and defects concentration (**Supporting Figure S23**). The enrichment of defects improves capacity retention, but excessive defects result in the loss of reversible capacity. As a result, $Li_{0.975}Ni_{1.025}O_2$ shows the best performance among the samples with different defects concentration. Note that good rate-capability is achieved for $Li_{0.975}Ni_{1.025}O_2$, which is comparable with $LiNiO_2$ (Fig. 5e), which is achieved by the suppression of particle size growth for the Li-deficient phase (**Supporting Figure S19**). These results suggest that Ni ion migration is partially mitigated by the presence of defects, and thus better electrode reversibility is achieved. Moreover, surface stability at the high voltage region is significantly improved using highly concentrated electrolyte solutions, leading to excellent capacity retention without the addition of non-Ni ions.

The suppression of Ni migration on charge is further supported through the analysis of phase evolution processes of $Li_{0.975-y}Ni_{1.025}O_2$ by *in-situ* XRD study. As shown in Fig. 5f, lattice parameter changes, especially for the expansion of the metal slabs on charge, are partly suppressed, similarly to $LiNiO_2$ with Li_3PO_4. The maximum difference for interlayer distances is reduced from 0.33 Å for $Li_{1-y}NiO_2$ to 0.30 for $Li_{0.975-y}Ni_{1.025}O_2$. Moreover, the increase in the peak intensity for 101 diffraction line is less evidenced, and similar peak profiles with those of $LiNiO_2$ with Li_3PO_4 are observed before and after charge to 4.5 V as compared in Fig. 5g. The peak shift of 110 diffraction line is also shown **Supporting Figure S24**. These findings clearly reveal that non-stoichiometric $Li_{0.975}Ni_{1.025}O_2$ with partial cation disordering and smaller grain size shows significantly better electrode performance compared with stoichiometric $LiNiO_2$, which originates from the suppression of Ni ion migration to tetrahedral sites on full delithiation.

In conclusions, unified understanding of detrimental phase transition in cobalt-free $LiNiO_2$ has been provided. $LiNiO_2$ integrated with nano-sized Li_3PO_4 derived from metastable rocksalt oxide shows excellent reversibility as electrode materials. The sample possesses 6 % anti-site defects in the structure, and the particle size is reduced to <100 nm with lower crystallinity. $LiNiO_2$ with analogous structural defects and particle size has been also directly synthesized through straightforward approach, *i.e.*, non-stoichiometric and Li deficient condition. Li deficient oxide, $Li_{0.975}Ni_{1.025}O_2$, shows excellent electrode reversibility in concentrated electrolyte with LiFSA. Ni migration to adjacent tetrahedral sites is effectively suppressed by the presence of extra Ni ions in Li layers, which is proofed by *in-situ* XRD study and theoretical DFT study. Extra Ni ions in Li layer also contribute less changes in interlayer distances on delithiation. Furthermore, unstable electrode surface on charge, presumably because of the destabilization of oxygen coupled with Ni migration [48], is effectively suppressed by using the highly

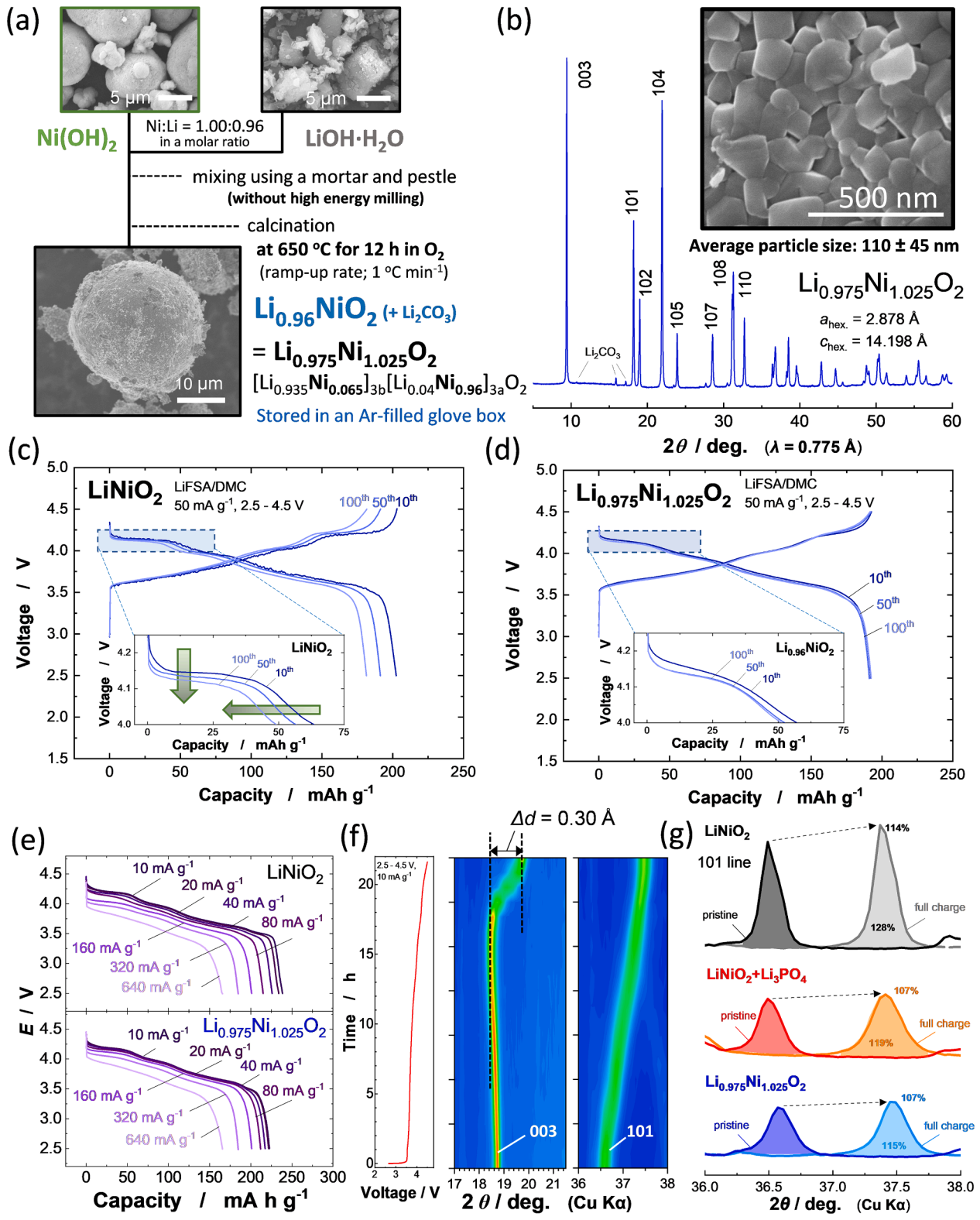

Fig. 5. Synthesis and characterization of Co-free $Li_{0.96}NiO_2$ ($Li_{0.975}Ni_{1.025}O_2$) with structural defects: (a) Scheme of synthesis for $Li_{0.96}NiO_2$, (b) a synchrotron XRD pattern and FE-SEM image of $Li_{0.975}Ni_{1.025}O_2$, galvanostatic charge/discharge curves of (c) Li/$LiNiO_2$ cell and (d) Li/ $Li_{0.975}Ni_{1.025}O_2$ cell at a rate of 50 mA g^{-1}; sample loading, (c) 3.43 and (d) 3.27 mg cm^{-2}, enlarged discharge curves are also shown in the insets, (e) rate capability of $LiNiO_2$ (loading; 3.40 mg cm^{-2}) and $Li_{0.975}Ni_{1.025}O_2$ (loading; 3.33 mg cm^{-2}), (f) contour plots for selected ranges of *in-situ* XRD patterns of $Li_{0.975}Ni_{1.025}O_2$ at a rate of 10 mA g^{-1}, and a corresponding initial charge curve, (g) comparison of intensity change for 101 diffraction line obtained from *in-situ* XRD patterns of different $LiNiO_2$ samples.

concentrated electrolyte solution. Note that the presence of defects is effective to improve the reversibility of the high voltage region associated with the suppression of Ni ion migration even though the defects negatively influence the electrode kinetics with 4.15 V cut-off, in which Ni migration cannot be observed (**Supporting Figure S22a**). This data also demonstrates the importance of defects in the high voltage region, coupled with Ni ion migration. In summary, significant improvement of electrode reversibility by simple approach is beneficial for practical and industrial applications, leading to the development of Co-free, high--performance, and cost-effective batteries in the future.

1. Experimental section

Synthesis of nanosized and rocksalt $LiNiO_2$ *integrated with* Li_3PO_4: $LiNiO_2$ was synthesized from a mixture of $LiOH{\cdot}H_2O$ and $Ni(OH)_2$. $LiOH{\cdot}H_2O$ (Wako Chemical Co.) was crushed into fine powder by using a mortar and pestle, and then mixed with $Ni(OH)_2$ (Wako Chemical Co.). 3 mol% excess $LiOH{\cdot}H_2O$ was used to compensate Li ion vaporization on heating. A mixture of $LiOH{\cdot}H_2O$ and $Ni(OH)_2$ was pressed into a pellet. The pellet was heated at 650 °C for 12 h under O_2 stream. Li_3PO_4 was purchased from Wako Chemical Co. 1.00 g of $LiNiO_2$ and 36.7 mg of Li_3PO_4 were mixed using a planetary ball mill (PULVERISETTE 7; FRITSCH) with a zirconia pot (45 mL) and balls (14.8 g) at 600 rpm. After milling, the sample was taken out from the container and mixed with a mortar and pestle to ensure sample uniformity during the milling after 12 h, and the total milling time was 24 h. Nanosized and rocksalt $LiNiO_2$ synthesized by high-energy milling was further heat treated at 650 °C for 6 h, leading to the formation of layered $LiNiO_2$ integrated with Li_3PO_4.

Synthesis of Li deficient Li_xNiO_2: Li_xNiO_2 ($1.00 \geq x \geq 0.90$) were synthesized from a mixture of $LiOH{\cdot}H_2O$ and $Ni(OH)_2$. $LiOH{\cdot}H_2O$ (Wako Chemical Co.) was crushed into fine powder by using a mortar and pestle, and then mixed with $Ni(OH)_2$ (Wako Chemical Co.). Molar ratios of the precursors were changed from Ni:Li = 1.00:1.00 to 1.00:0.90. Excess amount of $LiOH{\cdot}H_2O$ was not added for the synthesis of samples. Mixtures of $LiOH{\cdot}H_2O$ and $Ni(OH)_2$ were pressed into a pellet. The pellet was heated in a tube furnace under O_2 stream. Temperature of the furnace was ramped up at a rate of 1 °C min^{-1} to 650 °C, and then held at 650 °C for 12 h. After cooling, the pellet was stored in an Ar-filled glovebox. When it is assumed that cation vacancies are not formed and Li ions are not lost on heating, the chemical compositions of these samples are expected to be $Li_{1-x}Ni_{1+x}O_2$ ($0 \geq x \geq 0.05$). Note that a small amount of Li_2CO_3 is found in the samples, chemical compositions after heating are expected to be slightly deviated from these formulas.

Electrochemical characterization: Composite positive electrodes consisting of 80 wt% $LiNiO_2$, 10 wt% acetylene black (HS-100, Denka Co.), and 10 wt% polyvinylidene fluoride (KF 1100; Kureha Co.) dispersed in N-methylpyrrolidone were pasted on aluminum foil as a current collector. The electrodes were dried at 80 °C for 2 h in vacuum and then heated at 120 °C for 2 h. Metallic lithium (Honjo Metal Co.) was used as a negative electrode. Polyolefin porous membrane was used as separator. The electrolyte solution used was 1.0 mol dm^{-3} $LiPF_6$ dissolved in ethylene carbonate/dimethyl carbonate (3:7 by volume, battery grade; Kishida Chemical Co.). LiFSA:DMC = 1:1.1 in a molar ratio was also used as electrolyte (battery grade; Kishida Chemical Co.). Because LiFSA: DMC = 1:1.1 has high viscosity as electrolyte solution, electrolyte cannot soak through conventional polyolefin porous membrane. Therefore, polyolefin porous membrane, LIELSORT®, Teijin Ltd., which is coated on both side with the aramid layer [49], was used as separator. Detailed information of aramid-coated separator is also found in our recent publications [45,46]. Two-electrode cells (TJ-AC; Tomcell Japan) were assembled in the Ar-filled glovebox.

Structural and morphological characterization: Synchrotron X-ray diffraction (XRD) data were collected on the beamline BL19B2 at SPring-8 synchrotron facility in Japan [50]. The measurement was conducted using an automatic powder diffraction system for the Debye–Scherrer geometry by placing the sample in a glass capillary. The wavelength used was 0.500 Å, which was calibrated with CeO_2 as a reference sample. Structural analysis was carried out using RIETAN-FP [51]. Structural analysis of samples was also conducted by time-of-flight neutron diffraction (TOF-ND) measurement at iMATERIA [52], BL20 of Materials and Life Science Experimental Facility (MLF), J-PARC in Japan. The samples were sealed in vanadium tubes (6.0 mm in diameter) in an inert atmosphere. TOF-ND data was collected at room temperature. The collected data was analyzed using the Z-Rietveld software [53] Electron density distributions were calculated by maximum entropy method (MEM) using the crystal structure factors and standard deviations from the Rietveld analysis. All MEM analyses were carried out using the Z-MEM in the Z-Code software package [54]. Three-dimensional electron density maps are analyzed and visualized by the program VESTA [55].

Hard XAS spectra at the Ni K-edge was collected at beamline BL-12C of the Photon Factory Synchrotron Source in Japan. Hard XAS spectra were collected with a silicon monochromator in the transmission mode.

For scanning transmission electron microscopy coupled with energy dispersive X-ray spectroscopy (STEM–EDX), an electron microscope (Themis Z; Thermo Fisher Scientific Inc.) equipped with a dual EDX detector (XFlash® 6–100; Bruker Co.) was operated at 300 kV. The probe current, scan step, dwell time and total flames were set as 85 pA, 1.725 nm,12.5 μs and 472, respectively. A 3-pix average filter was used to obtain EDS net-intensity maps in Fig. 1. Samples were dispersed on a dried holey carbon film supported by a grid (R2/2 Cu; QUANTIFOIL) in an argon atmosphere. The grid was set on a vacuum transfer holder (Model 648; Gatan Inc.).

Field emission scanning electron microscopy (FE-SEM) was conducted by using a SU8010 (Hitachi High-Tech Corporation) operated at 10 kV. For cross-sectional observation of the samples, focused ion-beam (FIB) milling was used with a JIB-4501 (JEOL Ltd.). The sample was preliminarily covered with carbon. Gallium liquid metal ion source was used for milling. STEM-EDX observation for the cross-sectional observation in Fig. 2c was conducted on a JEM-2100F (JEOL Ltd.) operated at 200 kV. The sample prepared by FIB was transferred on a carbon-coated copper grid (SHR-C075; OKENSHOJI). EDX observation was conducted on a JED-2300T (JEOL Ltd.).

Density functional theory (DFT) calculations were performed by employing the Vienna *Ab initio* Simulation Package (VASP) [56] with the projector augmented wave (PAW) pseudopotentials [57]. Perdew-Burke-Ernzerhof (PBE) [58] generalized gradient approximation functional with the vdw-optPBE correction [59] and the Hubbard term U_{Ni} = 6.0 eV was applied to all of the calculations. The $2\sqrt{3}\times 2\sqrt{3}\times 1$ supercells of $[\square_{11/12}Li_{1/12}]_{3a}[Ni]_{3b}O_2$ ($Li_3Ni_{36}O_{72}$ with one Li ion in each Li layer) and $[\square_{11/12}Ni_{1/12}]_{3a}[Li_{1/12}Ni_{11/12}]_{3b}O_2$ with one Ni ion in each Li layer and one Li ion in each Ni layer were used. Cut-off energy of 520 eV and the *k*-point mesh of $2 \times 2 \times 1$ were used. The geometry relaxation calculations were converged until the residual forces were less than 2×10^{-2} eV $Å^{-1}$. The energy profiles of the Ni ion migration were examined using the climbing image nudged elastic band method (CI-NEB) [60,61]. The spring force between the images was set at −5 eV $Å^{-1}$ and the NEB calculations were converged when the NEB forces were smaller than 3×10^{-2} eV $Å^{-1}$.

CRediT authorship contribution statement

Itsuki Konuma: Data curation, Formal analysis, Writing – original draft. **Naohiro Ikeda:** Data curation, Formal analysis, Writing – original draft. **Benoît D.L. Campéon:** Methodology, Writing – review & editing. **Hinata Fujimura:** Data curation, Formal analysis. **Jun Kikkawa:** Methodology. **Huu Duc Luong:** Methodology, Writing – original draft. **Yoshitaka Tateyama:** Methodology, Writing – review & editing. **Yosuke Ugata:** Methodology. **Masao Yonemura:** Formal analysis, Methodology. **Toru Ishigaki:** Methodology. **Taira Aida:** Methodology.

Naoaki Yabuuchi: Conceptualization, Funding acquisition, Writing – review & editing.

Declaration of competing interest

The authors declare that they have no known competing financial interests or personal relationships that could have appeared to influence the work reported in this paper.

Data availability

Data will be made available on request.

Acknowledgments

NY acknowledges the partial support from JSPS, Grant-in-Aid for Scientific Research (Grant Numbers 19H05816 and 21H04698), and HDL and YT also thank JSPS (Grant Number 19H05815). This work was partially supported by JST, CREST Grant Number JPMJCR21O6, Japan and by MEXT Program: Data Creation and Utilization-Type Material Research and Development Project Grant Number JPMXP1122712807. The synchrotron X-ray absorption work was done under the approval of the Photon Factory Program Advisory Committee (Proposal No. 2021G039). The synchrotron radiation experiments were performed at the BL19B2 of SPring-8 with the approval of the Japan Synchrotron Radiation Research Institute (JASRI) (Proposal No. 2021B1722). The ND experiments at the Materials and Life Science Experimental Facility of the J-PARC were performed under a user program (Proposal No. 2019PM2004). NY also thanks Satoshi Nishikawa and Takayoshi Yamamoto from Teijin Ltd. for the supply of LIELSORT® separator. We thank Ms. Yuko Kaneda and Mr. Masashi Kondo of the Instrumental Analysis Center at Yokohama National University for their excellent technical support in using STEM-EDX.

Supplementary materials

Supplementary material associated with this article can be found, in the online version, at doi:10.1016/j.ensm.2024.103200.

References

[1] K. Mizushima, P.C. Jones, P.J. Wiseman, J.B. Goodenough, Mater. Res. Bull. 15 (1980) 783–789.
[2] E.A. Olivetti, G. Ceder, G.G. Gaustad, X. Fu, Joule 1 (2017) 229–243.
[3] N. Yabuuchi, Chem. Rec. 19 (2019) 690–707.
[4] J.R. Dahn, U. von Sacken, M.W. Juzkow, H. Al-Janaby, J. Electrochem. Soc. 138 (1991) 2207–2211.
[5] T. Ohzuku, A. Ueda, M. Nagayama, J. Electrochem. Soc. 140 (1993) 1862–1870.
[6] H. Arai, M. Tsuda, K. Saito, M. Hayashi, K. Takei, Y. Sakurai, J. Solid State Chem. 163 (2002) 340–349.
[7] C.S. Yoon, D.-W. Jun, S.-T. Myung, Y.-K. Sun, ACS Energy Lett. 2 (2017) 1150–1155.
[8] M. Hata, T. Tanaka, D. Kato, J.-H. Kim, S. Yonezawa, Electrochemistry 89 (2021) 223–229.
[9] B.D.L. Campéon, N. Yabuuchi, Chem. Phys. Rev. 2 (2021) 041306.
[10] D. Weber, J. Lin, A. Pokle, K. Volz, J. Janek, T. Brezesinski, M. Bianchini, J. Electrochem. Soc. 169 (2022) 030540.
[11] R. Qiu, Z. Wu, Electrochemistry 89 (2021) 296–302.
[12] W. Ge, Y. Fu, X. Ma, X. Li, G. Peng, Energy Adv. 1 (2022) 28–37.
[13] A. Aishova, G.-T. Park, C.S. Yoon, Y.-K. Sun, Adv. Energy Mater. 10 (2020) 1903179.
[14] C. Geng, A. Liu, J.R. Dahn, Chem. Mater. 32 (2020) 6097–6104.
[15] H. Li, M. Cormier, N. Zhang, J. Inglis, J. Li, J.R. Dahn, J. Electrochem. Soc. 166 (2019) A429–A439.
[16] N. Ikeda, I. Konuma, H.B. Rajendra, T. Aida, N. Yabuuchi, J. Mater. Chem. A 9 (2021) 15963–15967.
[17] H. Li, N. Zhang, J. Li, J.R. Dahn, J. Electrochem. Soc. 165 (2018) A2985–A2993.
[18] Z. Chen, Z. Lu, J.R. Dahn, J. Electrochem. Soc. 149 (2002) A1604.
[19] G.G. Amatucci, J.M. Tarascon, L.C. Klein, J. Electrochem. Soc. 143 (1996) 1114–1123.
[20] U.H. Kim, D.W. Jun, K.J. Park, Q. Zhang, P. Kaghazchi, D. Aurbach, D.T. Major, G. Goobes, M. Dixit, N. Leifer, C.M. Wang, P. Yan, D. Ahn, K.H. Kim, C.S. Yoon, Y. K. Sun, Energy Environ. Sci. 11 (2018) 1271–1279.
[21] H.-H. Ryu, G.-T. Park, C.S. Yoon, Y.-K. Sun, J. Mater. Chem. A 7 (2019) 18580–18588.
[22] C. Geng, D. Rathore, D. Heino, N. Zhang, I. Hamam, N. Zaker, G.A. Botton, R. Omessi, N. Phattharasupakun, T. Bond, C. Yang, J.R. Dahn, Adv. Energy Mater. 12 (2022) 2103067.
[23] M. Sawamura, S. Kobayakawa, J. Kikkawa, N. Sharma, D. Goonetilleke, A. Rawal, N. Shimada, K. Yamamoto, R. Yamamoto, Y. Zhou, Y. Uchimoto, K. Nakanishi, K. Mitsuhara, K. Ohara, J. Park, H.R. Byon, H. Koga, M. Okoshi, T. Ohta, N. Yabuuchi, ACS Cent. Sci. 6 (2020) 2326–2338.
[24] R. Fukuma, M. Harada, W. Zhao, M. Sawamura, Y. Noda, M. Nakayama, M. Goto, D. Kan, Y. Shimakawa, M. Yonemura, N. Ikeda, R. Watanuki, H.L. Andersen, A. M. D'Angelo, N. Sharma, J. Park, H.R. Byon, S. Fukuyama, Z. Han, H. Fukumitsu, M. Schulz-Dobrick, K. Yamanaka, H. Yamagishi, T. Ohta, N. Yabuuchi, ACS Cent. Sci. 8 (2022) 775–794.
[25] H.S. Liu, Z.R. Zhang, Z.L. Gong, Y. Yang, Electrochem. Solid-State Lett. 7 (2004) A190.
[26] A. Rougier, P. Gravereau, C. Delmas, J. Electrochem. Soc. 143 (1996) 1168–1175.
[27] N. Yabuuchi, S. Kumar, H.H. Li, Y.-T. Kim, Y. Shao-Horn, J. Electrochem. Soc. 154 (2007) A566.
[28] N. Yabuuchi, K. Yoshii, S.-T. Myung, I. Nakai, S. Komaba, J. Am. Chem. Soc. 133 (2011) 4404–4419.
[29] F. Kong, C. Liang, R.C. Longo, Y. Zheng, K. Cho, J. Power Sources 378 (2018) 750–758.
[30] D. Eum, B. Kim, S.J. Kim, H. Park, J. Wu, S.-P. Cho, G. Yoon, M.H. Lee, S.-K. Jung, W. Yang, W.M. Seong, K. Ku, O. Tamwattana, S.K. Park, I. Hwang, K. Kang, Nat. Mater. 19 (2020) 419–427.
[31] J. Huang, B. Ouyang, Y. Zhang, L. Yin, D.-H. Kwon, Z. Cai, Z. Lun, G. Zeng, M. Balasubramanian, G. Ceder, Nat. Mater. 22 (2023) 353–361.
[32] Y. Kim, Phys. Chem. Chem. Phys. 21 (2019) 24139–24146.
[33] C.S. Yoon, M.-J. Choi, D.-W. Jun, Q. Zhang, P. Kaghazchi, K.-H. Kim, Y.-K. Sun, Chem. Mater. 30 (2018) 1808–1814.
[34] W. Yang, H. Li, D. Wang, C. Xu, W. Xiang, Y. Song, F. He, J. Zhang, B. Zheng, B. Zhong, Z. Wu, X. Guo, Nano Energy 104 (2022) 107880.
[35] M. Hofmann, F. Nagler, M. Kapuschinski, U. Guntow, G.A. Giffin, ChemSusChem 13 (2020) 5962–5971.
[36] F. Du, X.-f. Bie, X.-f. Bian, F. Hu, G. Chen, C.-z. Wang, Y.-j. Wei, Chem. Res. Chin. Univ. 29 (2013) 210–213.
[37] E.D. Orlova, A.A. Savina, S.A. Abakumov, A.V. Morozov, A.M. Abakumov, Symmetry (Basel) 13 (2021) 1628.
[38] T. Yamada, Y. Kamiya, N. Naruse, N. Zettsu, K. Teshima, Cryst. Growth Des. 19 (2019) 5720–5728.
[39] N. Yabuuchi, K. Kubota, Y. Aoki, S. Komaba, J. Phys. Chem. C 120 (2016) 875–885.
[40] N. Phattharasupakun, M.M.E. Cormier, E. Lyle, E. Zsoldos, A. Liu, C. Geng, Y. Liu, H. Li, M. Sawangphruk, J.R. Dahn, J. Electrochem. Soc. 168 (2021) 090535.
[41] J. Wang, Y. Yamada, K. Sodeyama, C.H. Chiang, Y. Tateyama, A. Yamada, Nat. Commun. 7 (2016) 12032.
[42] J. Wang, Y. Yamada, K. Sodeyama, E. Watanabe, K. Takada, Y. Tateyama, A. Yamada, Nat. Energy 3 (2018) 22–29.
[43] Y. Ugata, R. Tatara, T. Mandai, K. Ueno, M. Watanabe, K. Dokko, ACS Appl. Energy Mater. 4 (2021) 1851–1859.
[44] W. Xu, H. Wang, Y. Gao, Y. Wei, H. Zhang, C. Gao, F. Kang, D. Zhai, Energy Adv. 1 (2022) 191–196.
[45] N. Shimada, Y. Ugata, S. Nishikawa, D. Shibata, T. Ohta, N. Yabuuchi, Energy Adv. 2 (2023) 508–512.
[46] Y. Ugata, C. Motoki, S. Nishikawa, N. Yabuuchi, Energy Adv. 2 (2023) 503-507.
[47] R. Pan, E. Jo, Z. Cui, A. Manthiram, Adv. Funct. Mater. 33 (2023) 2211461.
[48] W.E. Gent, K. Lim, Y. Liang, Q. Li, T. Barnes, S.-J. Ahn, K.H. Stone, M. McIntire, J. Hong, J.H. Song, Y. Li, A. Mehta, S. Ermon, T. Tyliszczak, D. Kilcoyne, D. Vine, J.-H. Park, S.-K. Doo, M.F. Toney, W. Yang, D. Prendergast, W.C. Chueh, Nat. Commun. 8 (2017) 2091.
[49] Y. Nagao, M. Sato, M. Okazaki, S. Nishikawa, in, 2020.
[50] K. Osaka, Y. Yokozawa, Y. Torizuka, Y. Yamada, M. Manota, N. Harada, Y. Chou, H. Sasaki, A. Bergamaschi, M. Sato, AIP Conf. Proc. 2054 (2019) 050008.
[51] F. Izumi, K. Momma, Solid State Phenom. 130 (2007) 15–20.
[52] T. Ishigaki, A. Hoshikawa, M. Yonemura, T. Morishima, T. Kamiyama, R. Oishi, K. Aizawa, T. Sakuma, Y. Tomota, M. Arai, M. Hayashi, K. Ebata, Y. Takano, K. Komatsuzaki, H. Asano, Y. Takano, T. Kasao, Nucl. Instrum. Methods Phys. Res., Sect. A 600 (2009) 189–191.
[53] R. Oishi, M. Yonemura, Y. Nishimaki, S. Torii, A. Hoshikawa, T. Ishigaki, T. Morishima, K. Mori, T. Kamiyama, Nucl. Instrum. Methods Phys. Res. A 600 (2009) 94–96.
[54] Y. Ishikawa, J. Zhang, R. Kiyanagi, M. Yonemura, T. Matsukawa, A. Hoshikawa, T. Ishigaki, S. Torii, R. Oishi-Tomiyasu, T. Kamiyama, Phys. B: Condens. Matter 551 (2018) 472–475.
[55] K. Momma, F. Izumi, J. Appl. Crystallogr. 44 (2011) 1272–1276.
[56] G. Kresse, J. Hafner, Phys. Rev. B Condens. Matter 47 (1993) 558–561.
[57] G. Kresse, D. Joubert, Phys. Rev. B 59 (1999) 1758–1775.
[58] J.P. Perdew, K. Burke, M. Ernzerhof, Phys. Rev. Lett. 77 (1996) 3865–3868.
[59] J. Klimes, D.R. Bowler, A. Michaelides, J. Phys. Condens. Matter 22 (2010) 022201.
[60] D. Sheppard, P. Xiao, W. Chemelewski, D.D. Johnson, G. Henkelman, J. Chem. Phys. 136 (2012) 074103.
[61] G. Henkelman, B.P. Uberuaga, H. Jónsson, J. Chem. Phys. 113 (2000) 9901–9904.